# Incorporating the G-TFSF Concept into the Analytic Field Propagation TFSF Method

John B. Schneider, *Senior Member, IEEE*, and Zhen Chen, *Student Member, IEEE*

***Abstract*—Previously, Anantha and Taflove reported a generalized total-field/scattered-field (G-TFSF) formulation that was developed to facilitate the study of infinite scatterers, such as wedges [*IEEE Trans. Antennas and Propag.*, vol. 50, no. 10, 1337–1349, Oct. 2002]. The G-TFSF formulation relied upon having the TFSF boundary embedded within a perfectly matched layer (PML). To account for the PML, the incident-field terms that appear in the update equations for nodes adjacent to the TFSF boundary were scaled by a constant in accordance with the amount of attenuation produced by the PML. In this work we describe how the analytic field propagation TFSF (AFP TFSF) formulation can be used in a G-TFSF-like way. This new approach possesses various advantages over the previously presented work. For example, owing to the dispersion inherent in PML's, the spectral components of pulsed excitation propagate at the different speeds within the PML. This dispersive behavior can be accommodated in the AFP-based formulation but not in the original G-TFSF implementation. Additionally, the AFP-based technique can directly model the infinite nature of objects, such as wedges, so that corners need not be embedded within the PML.**

***Index Terms*—FDTD methods.**

## I. Introduction

In finite-difference time-domain (FDTD) simulations the total-field/scattered-field (TFSF) boundary separates the computational grid into two regions: a total-field region (that contains the incident and scattered fields) and a scattered-field region (that contains only the scattered field). In addition to confining the incident field within the total-field region, the TFSF boundary can, in principle, be used to introduce any type of incident field into the FDTD grid. In practice, however, the TFSF boundary is used almost exclusively to introduce plane wave excitation.

The original formulations of the TFSF boundary date back to the early 1980's [1], [2]. The TFSF boundary is implemented by subtracting the incident field from, and adding the incident field to, the update equation for nodes that are both adjacent to and tangential to the boundary (addition is done to nodes on one side of the boundary while subtraction is done to those on the other side). These incident-field terms act like the currents in an equivalence principle formulation or the sources surrounding a Huygens surface. For non-grid-aligned incidence, the major source of error in the implementation of TFSF boundaries is the mismatch between how fields propagate in the FDTD grid and how the incident field propagates (in whatever form the incident field is specified). If one uses the expression for the incident field that pertains to the continuous world, this mismatch can cause significant spurious fields to leak across the TFSF boundary. Alternatively, the incident field can be obtained from a one-dimensional (1D) "auxiliary-grid" FDTD simulation where the sole purpose of the auxiliary grid is to model the propagation of the incident field. For grid-aligned incidence in 2D and 3D, this auxiliary-grid approach works perfectly: no fields leak from the boundary since the dispersion in the auxiliary grid and the dispersion experienced by the incident field in the higher-dimensional grid are exactly the same. Unfortunately, for non-grid-aligned (oblique) incidence, although the traditional auxiliary-grid approach is very computationally efficient, fields will leak from the boundary and in some applications these leaked fields may be excessively large. An excellent description of both the general implementation of a TFSF boundary and the implementation of a 1D auxiliary grid can be found in [3].

Various authors have sought ways to improve the "traditional" auxiliary-grid approach mentioned above. Guiffaut and Mahdjoubi modified the auxiliary 1D grid so that the dispersion relationship governing the 1D grid was nearly the same as that for the obliquely propagating wave in the higher-dimensional grid [4]. This approach was limited in that, like the traditional approach, it still relied upon interpolation of the fields at nodes in the 1D grid to obtain fields at points corresponding to the projected location of nodes in the higher-dimensional grid. Other authors considered ways in which the errors caused by interpolation could be reduced [5], [6]. Nevertheless, there are some sources of error (leakage) that simply cannot be addressed by the traditional auxiliary-grid approach such as the fact that, unlike in the continuous world, for oblique incidence the fields in the FDTD grid are not completely orthogonal to the propagation vector.

An alternative 1D approach was recently put forward by Tan and Potter [7]. The 1D grid Tan and Potter developed had the same dispersion relationship as the higher-dimensional grid and, importantly, the nodes in the 1D grid are located precisely so that interpolation is not needed to obtain the fields in the higher-dimensional grid. This approach is attractive in many ways but currently it cannot be used for half-space problems (which is relevant to the work considered here) and it also requires that the incident angle be represented by a rational number (and the computational efficiency is related to this rational number).

Manuscript received December 04, 2010; accepted January 27, 2011. Date of publication July 12, 2011; date of current version September 02, 2011.

The authors are with the School of Electrical Engineering and Computer Science, Washington State University, Pullman, WA 99164-2752 USA (e-mail: schneidj@eecs.wsu.edu; zchen@eecs.wsu.edu).

Color versions of one or more of the figures in this paper are available online at http://ieeexplore.ieee.org.

Digital Object Identifier 10.1109/TAP.2011.2161452

Instead of using an auxiliary simulation to obtain the incident field, various authors derived an analytic description for the propagation of a (pulsed) plane wave in the FDTD grid [8]–[12]. This approach, which we identify as the analytic field propagation (AFP) TFSF method, allows fields to be incident at any angle and yet the resulting leakage is negligible. Furthermore, half-space problems can be modeled in which the transmitted and reflected fields associated with that half-space problem are also described analytically and confined to the total-field region. (In fact, the AFP TFSF method can even be used when the incident angle is beyond the critical angle and hence the transmitted field is evanescent [12].)

The AFP TFSF method is implemented by first obtaining, via a Fourier transform, the spectral description of the incident field at a single point in the grid. Then, given this "input" and using the FDTD dispersion relationship as the transfer function [13], [14], the spectral description of the incident field can be found at any other point in the grid. One then merely has to take the inverse Fourier transform of the product of the input and the transfer function to obtain the time-domain description of the incident field. This calculation is performed for every node that is tangential to, and adjacent to, the TFSF boundary. Implementation details can be found in [8]–[12]. For half-space problems, in addition to the usual incident or "incoming" wave, one must also calculate the reflected and transmitted fields. They are obtained in much the same way as the incoming field: one simply needs to include in the spectral description of the field the reflection coefficient or the transmission coefficient (which are themselves frequency dependent in the FDTD world). For the reflected field there is a slight change in the transfer function from that which pertains to the incoming field since the reflected field propagates away from the interface rather than toward it (hence there is sign change in the normal component of propagation). For the transmitted field the dispersion relation that gives the transfer function is that which governs propagation in the medium on the other side of the interface from the incident field.

In 2002 Anantha and Taflove reported what they called a generalized TFSF (G-TFSF) formulation [15] in which the total-field/scattered-field boundary was partially embedded in the perfectly matched layer (PML) [16] that was used to terminate the grid. If the incident field was propagating from the non-PML region toward the embedded TFSF boundary, the incident field terms in the update equations were scaled by an attenuation constant that was based on the amount of attenuation introduced by the PML. On the other hand, if the incident field originated on the embedded TFSF boundary and from there propagated toward the interior of the grid, the incident field terms were scaled by an amplification factor that compensated for the amount of attenuation the fields experienced when passing through the PML on their way to the interior of the grid.

Anantha and Taflove recognized that one could not simply use the continuous-world expression to determine the amount of attenuation a field would experience in an FDTD simulation. Instead the attenuation constants were obtained via calibration simulations in which a pulse was incident, at the particular angle of interest, on a PML and then the amount of attenuation measured at the appropriate locations. The amplification constant was the inverse of the attenuation constant. Anantha and Taflove stated that "the wave in the PML region propagates normally to the electric field with the speed of light in vacuum and undergoes an exponential decay with PML depth" [15]. Although this is true in the continuous world, it is not true in the discretized world of the FDTD grid. Instead, the PML region, like the rest of the grid, is dispersive. If the effect of the PML on the incident field is to be represented by a single attenuation constant, one has no choice but to ignore this dispersive behavior. However, using the AFP implementation of a TFSF boundary the incident field is, at an intermediate step, broken into its spectral representation. At that point the dispersive nature of the PML can be included.

In order to correct for both the amplitude and phase change caused by the presence of the PML, it is necessary that the calibration consist of two auxiliary simulations that record the full time-domain fields at the appropriate points. In the work by Anantha and Taflove only one auxiliary simulation was used for a particular incident angle. In the AFP-based implementation, one auxiliary simulation is done with the PML present at the nodes of interest and another simulation is done with the PML removed from these nodes. The two sets of time-domain fields are Fourier transformed to the frequency domain where the spectrum of the field with the PML is normalized by the spectrum of the field obtained without the PML. This gives the transfer function representing the effect of the PML. It is then a simple matter to incorporate this transfer function into the AFP TFSF method.

The original G-TFSF formulation modeled infinite scatterers, such as wedges, by partially embedding a finite scatterer in the PML and then having the G-TFSF boundary surround that. In this way the scattering from the PML-embedded edges and corners of the finite scatterer (i.e., the edges and corners that do not exist in the corresponding infinite scatterer) could be negligibly small since these scattered fields would have to propagate through the PML before entering the interior of the grid. As will be shown, there is no need for the construction of such finite scatterers when using the AFP TFSF boundary. Since the AFP TFSF method has already been formulated to directly handle half-space problems, this capability can be used to model scattering from wedges even though wedges are not truly half-space problems. Thus, it is not necessary for the TFSF boundary to be four-sided. In fact, it can be two-sided with two edges extending into the PML or, in the case of some perfect electric conductor (PEC) scatterers, only one edge extending into the PML.

The remainder of the paper is organized as follows. In Section II we demonstrate how calibration is performed and show that the dispersive nature of the PML is an important consideration when embedding a TFSF boundary within the PML. (We should note that in Anantha and Taflove's original work [15] they used a split-field PML in accordance with the one first presented by Bérenger [16]. In this work we use an unsplit complex frequency-shifted perfectly matched layer (CPML) formulation employing recursive convolution [17].) That is followed by a section that describes more general geometries and discusses the how calibration is done when the TFSF boundary is embedded in a PML that is itself in a dielectric associated with a half-space problem. Results are then provided to show

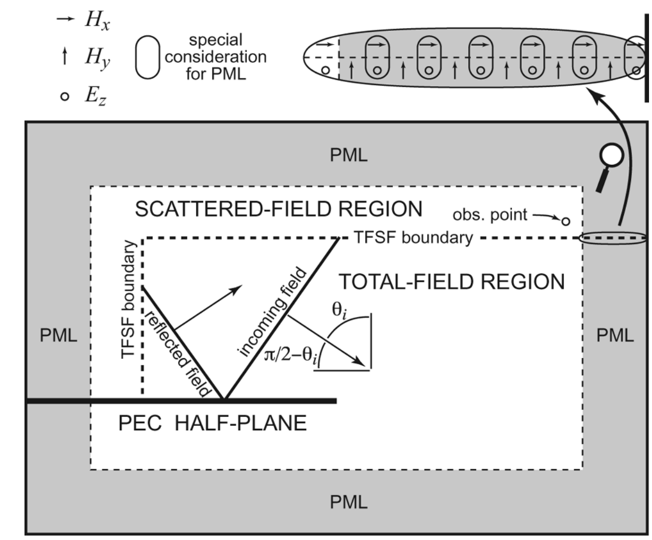


Fig. 1. Depiction of the $\mathrm{TM}_z$ illumination of a PEC half-plane using a two-sided AFP TFSF boundary. The portion of the TFSF boundary that extends into the PML on the right side of the grid is enclosed in an oval. The expanded view shows the $E_z$, $H_x$, and $H_y$ nodes along this boundary. Only the fields tangential to the boundary are involved in the TFSF formulation. Thus, for this horizontal edge, those are the $E_z$ and $H_x$ nodes. The TFSF nodes within the PML require special consideration and are shown as encircled pairs. The incident angle $\theta_i$ is defined with respect to the PEC surface normal.

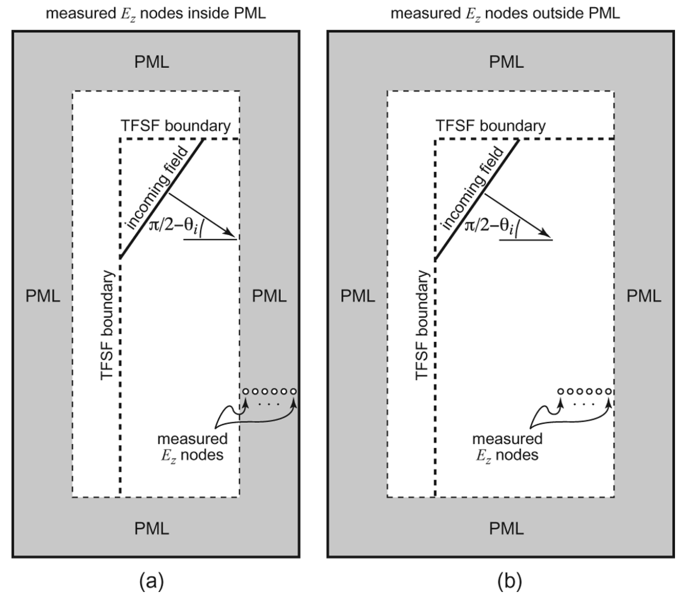


Fig. 2. Auxiliary simulations used for calibrating the AFP-based G-TFSF implementation. (a) The measured nodes are embedded inside the PML. (b) The measured nodes are outside the PML.

the improvements offered by the approach being advocated here. Additionally, to demonstrate the type of problems that can be addressed with this technique, some snapshots are shown from a simulation involving the termination of a dielectric halfspace in a 90 degree corner. We then conclude.

## II. Calibrating Both Magnitude and Phase

Let us start by considering oblique illumination of a PEC knife-edge, or half-plane, as shown in Fig. 1. As mentioned previously, in the AFP TFSF formulation the "incident field" consists of both the "incoming field" (i.e., what is typically called the incident field) *and* the reflected field. Were the PEC to span the entire domain, there would be no scattered field. The scattered field in this geometry is produced solely by the termination of the PEC. Thus, the incident field corresponds to that of illumination of an infinite plane wave. The incident angle $\theta_i$ is defined with respect to the normal to the PEC surface. Since the "incoming angle" and reflected angle are equal in magnitude, the behavior of both the incoming field and the reflected field at the PML can be characterized by this single angle.

As shown in Fig. 1, the TFSF boundary is two-sided. One side, the vertical one to the left of the figure, extends from the PEC to a point within the interior of the grid (by interior we mean points not within the PML). The other side is horizontal and extends from the top of the vertical boundary to the right edge of the grid. Thus this horizontal boundary passes through the PML region. The expanded view presented at the top of the figure shows the nodes along this edge. The $E_z$ and $H_x$ nodes adjacent to the TFSF boundary and within the PML are paired together with an enclosing oval. Note that the field is incident on the PML on the right side of the grid at an angle of $\pi/2-\theta_i$.

Naturally, special consideration is needed to calculate the incident field at the nodes within the PML. This involves two separate calibration runs. The calibration data determine the PML transfer function based on the "depth" of a node in the PML. The transfer function is the same for both electric- and magnetic-field nodes provided they are at the same depth. Thus, the $E_z$ and $H_x$ pairs shown in Fig. 1 have the same transfer function.

One could potentially derive a completely analytic description of the effect of the PML. Some authors have developed expressions for the reflection and transmission coefficients associated with a discretized PML (see, for example, [18]–[21]). However, owing to the complexity of performing a completely analytic description of a multilayer CPML, that was not attempted here. Instead, as was done in [15], we simply do auxiliary computations (i.e., calibration runs) where the sole purpose is to measure the effect of the PML.

For a given PML geometry, a calibration needs to be performed only once but it is a function of the incident angle. Hence, if the incident angle changes, another calibration needs to be performed. In [15], the goal was to obtain a scalar constant that was subsequently used to scale the incident-field terms in the update equations for nodes tangentially adjacent to the TFSF boundary and in the PML. For a given incident angle, the constant was a function of only the depth of a node within the PML.

In the AFP-based implementation, two auxiliary FDTD simulations are done: one with the nodes of interest embedded in the PML and one where the PML is removed from these nodes. This is illustrated in Fig. 2. Fig. 2(a) depicts the simulation where the nodes of interest (i.e., the measured nodes) are embedded in the PML. The measured nodes form a line that spans the PML and is normal to the edge of the grid. One can measure either electric or magnetic fields (in our work we used electric fields). In this simulation there is only an "incoming" field which originates from the upper-left corner of the total-field region. The distance between the vertical TFSF boundary and the PML on the right side of the domain is unimportant—it can be as small as a single cell. For this simulation, the horizontal TFSF boundary, shown near the top of the figure, does not extend into the PML. Thus, there is some spurious radiation from the termination of this boundary. Owing to the oblique incidence (which produces a vertical phase velocity of the incoming field greater than the speed of light), the incoming field arrives at the measured nodes prior to this spurious radiation. Therefore the spurious radiation can be (and is) time-gated out of the measured data. (The computational domain must be of sufficient size to allow this temporal separation to occur. This time-gating approach is not absolutely necessary as one could extend the horizontal TFSF boundary into the PML, but it would take multiple calibrations runs to do this. As will be shown, the calibration data obtained from the two auxiliary simulations depicted in Fig. 2 were sufficiently accurate that no further refinement was deemed necessary.)

Fig. 2(b) depicts the simulation where the measured nodes are *not* embedded in the PML. The only difference between this simulation and the one depicted in Fig. 2(a) is that the computational domain is expanded to the right. The distance from the measured nodes to the TFSF boundary remains unchanged and all the parameters pertaining to the incident field are unchanged. (In theory, to obtain a transfer function that describes only the effect of the PML, in the simulation shown in Fig. 2(b), the right side of the computational domain should be made distant enough that any reflection from the termination of the right side of the grid does not return to measurement points over the duration of the observation. However, in practice, reflections from the PML on the right were found to be small enough that isolating them from the transfer function did not have an appreciable effect on the quality of the final results. Thus, in the results to be shown later, the geometry we used for the second calibration run was similar to the depiction in Fig. 2(b)—the right-side PML was just beyond the measurement points.)

We are interested in the effect the PML has on both the magnitude *and* the phase of the incident field. Thus the entire temporal history at each measured electric-field node in the PML is recorded. The time-domain data are transformed to the frequency domain. The spectral representation of the field for nodes embedded in the PML is normalized by the spectrum of the field at the same node but without the PML. Said another way, the data obtained from Fig. 2(a) are normalized by the data obtained from Fig. 2(b). These normalized spectral data, one set per electric-field node, are the transfer functions that can be used directly in the AFP-based G-TFSF formulation to model the effect of the PML.

If the time-domain field with the PML is $E_z^p(x,y,t)$ while the field without the PML is $E_z^w(x,y,t)$, the transfer function is given by

$$G(x,y,\omega) = \frac{\mathcal{F}\left[E_z^p(x,y,t)\right]}{\mathcal{F}\left[E_z^w(x,y,t)\right]}. \qquad (1)$$

where $\mathcal{F}[]$ is the Fourier transform. The transfer function $G(x,y,\omega)$ would be used, for instance, in Eqs. (45)–(47) in [11] to account for the presence of the PML. However, in our implementation we used a slightly simplified approximation of the transfer function as will be described.

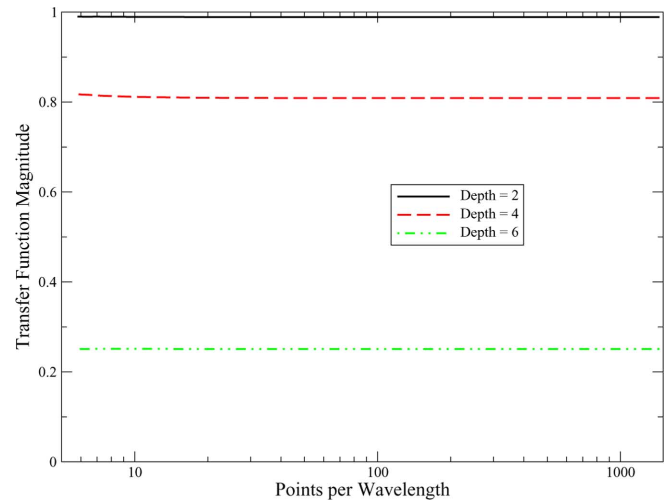


Fig. 3. Magnitude of the transfer function as a function of discretization at depths of 2, 4, and 6 cells into the PML.

Fig. 3 shows the magnitude of the PML transfer function vs. discretization when measured at a cell that is at a depth of either 2, 4, or 6 cells (the overall thickness of the PML is 8 cells). There were 2048 time-steps in the simulation (zero-padding was used after the time-gating to obtain the desired number of points). The simulations were run at the 2-D Courant limit of $1/\sqrt{2}$. This plot correspond to the first 249 non-dc frequency bins after Fourier transforming the time-domain data. Thus, the lowest non-dc frequency corresponds to approximately 1448 points per wavelength while the highest frequency corresponds to approximately 5.8 points per wavelength. (The discretization is given by $2048/(N_f\sqrt{2})$ where $N_f$ is the bin number. An $N_f$ of zero corresponds to dc.) From Fig. 3 one see that the transfer function magnitude is nearly (but not perfectly) constant with respect to frequency (or discretization). Thus, the attenuation experienced by fields as they propagate into the PML is nearly independent of frequency. This is the basis of the implementation that Anantha and Taflove [15] where a single constant was used to describe the effect of the PML. However, phase is not independent of frequency.

Fig. 4 shows the phase of the transfer function as a function of frequency or, more precisely, frequency bin. The data shown are for the same depths and span the same discretizations as shown in Fig. 3. The phase of the transfer function represents the difference in phase between when the PML is and is not present. If one is to use a real constant to model the transfer function, ideally the phase of the transfer function would be zero for all frequencies.

At a depth of 2 cells, the phase of the transfer function remains very small, varying from approximately 0.0017 degrees at 1448 points per wavelength ($N_f = 1$) to just under 0.357 degrees at 5.8 points per wavelength ($N_f = 249$). This amount of phase difference would not be a practical concern in most applications. However, as seen in Fig. 4, at greater depths, the phase change imparted by the PML can be much more substantial. The phase shift is nearly 35 degrees at a depth of 6 cells and a discretization of 5.8 points per wavelength. For a PML of typical size (i.e., in the neighborhood of eight cells), to obtain a high-fidelity simulation where the penetration of the TFSF boundary

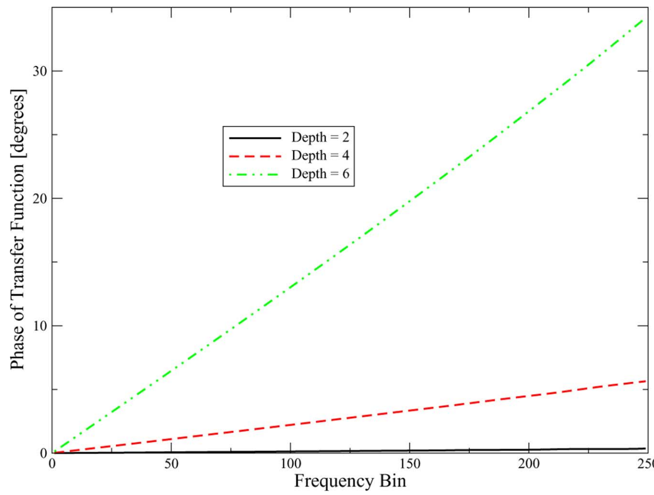


Fig. 4. Phase of the transfer function as a function of frequency at depths of 2, 4, and 6 cells into the PML.

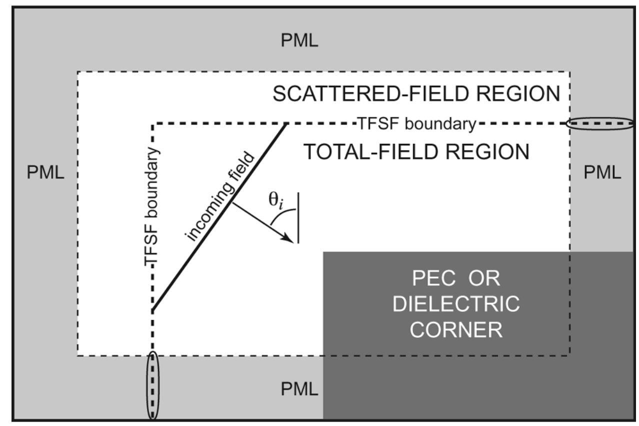


Fig. 5. A corner illuminated by a field that first encounters the edge of the corner, i.e., the incident field originated in the homogeneous space to the left of the corner. The two places where the TFSF boundary passes into the PML are enclosed in an oval.

into PML does not cause significant spurious radiation, it is necessary to account for this phase shift.

In principle, it is possible to measure the magnitude and phase of the transfer function at each spectral bin and use that in a given simulation. However, we use a simplified approximation to the transfer function that still provides excellent fidelity. Like Anantha and Taflove, we use a constant for the magnitude. For a given depth, this constant is obtained by averaging a portion of the data shown in Fig. 3. (The average is taken over frequencies that fall within the full-width half-maximum spectrum of the Ricker wavelet pulse that was used for illumination. This effectively discards the highest and lowest frequencies from the average.) For the phase, one notes from Fig. 4 that the phase varies nearly (but not perfectly) linearly with frequency. Thus, we fit a straight line to the phase data shown in Fig. 4. These simplifications allows the calibration data to be decoupled from the duration of the actual simulation of interest. Thus, knowing that the magnitude is constant and the phase varies linearly, one can easily calculate the transfer-function coefficient for any frequency of interest (and it will not matter if the calibration data were calculated with 2048 time-steps while the simulation of interest may use, for example, 5000 time-steps or any other value).

(In the CPML implementation used here, the maximum conductivity was obtained from (7.66) of [3] with a polynomial grading exponent of $m = 3$. The $\kappa$ and $\alpha$ (or $a$) parameters that can be used to tune a CPML were set to 1.0 and 0.0, respectively. PML parameters other than the ones we employed may make it so that the magnitude is not approximated well by a constant or the phase variation is not approximated well by simple linear variation. That does not change the basic underlying approach being advocated here. For such cases one can simply approximate the frequency-dependent variations in magnitude and phase with higher-order functions, i.e., functions other than a constant or straight line.)

In the standard AFP TFSF method the entire time-domain description of the incident field at every node adjacent to the TFSF boundary is pre-computed, stored, and then recalled as needed during the time-stepping of an FDTD simulation. The fact that the incident field in an AFP G-TFSF simulation contains both the incoming and the reflected fields does not change the way calibration is done. As indicated previously, this is a consequence of the angle of reflection being equal to the angle of incidence: the way in which the PML affects the magnitude and phase of these two fields is the same.

## III. Other Geometries

For the knife-edge problem shown in Fig. 1, the geometry of the TFSF boundary would not change if, say, one wanted to consider the diffraction from a 90-degree PEC corner. In fact, the corner could have any angle from 0 degrees (the knife-edge problem) to 180 degrees (a perfectly flat plane). However, the geometry does change if the incident angle is such that the incoming field encounters the edge before the rest of the half-plane. This scenario is depicted in Fig. 5 where the corner is illuminated by a plane wave that originates in the homogeneous region to the left of the corner. (We will identify this as the free space region even though it could be any homogeneous dielectric material.)

In Fig. 5 the corner is drawn as a 90-degree corner, but any angle is permissible. Furthermore, the corner material is arbitrary. It could either be a PEC or dielectric. In this scenario there is no reflected plane wave: the incident field is comprised solely of the "incoming field." The TFSF boundary is again two-sided but now each side passes through the PML and is terminated at the edge of the grid. Both these edges are in the free-space region. Two sets of calibration need to be performed to account for the fact that the edges are orthogonal to each other. Nevertheless, the way in which calibration is done is essentially unchanged from the description in the previous section. The only change is the angle of the incoming field.

Using a two-sided PML, it is also possible to model the illumination of a dielectric corner when the incident field originates in the half-space region. This is depicted in Fig. 6 where the incident field is introduced from the left and consists of the incoming field, the reflected field, and the transmitted field. In this case one side of the TFSF boundary is terminated in the PML in the dielectric (at the bottom of the figure) and the other side is terminated in the PML in free space (along the right side of the figure).

For the case of a penetrable dielectric as shown in Fig. 6, the calibration must be performed in a slightly different way than depicted in Fig. 2. Instead, the calibration set-up is as shown

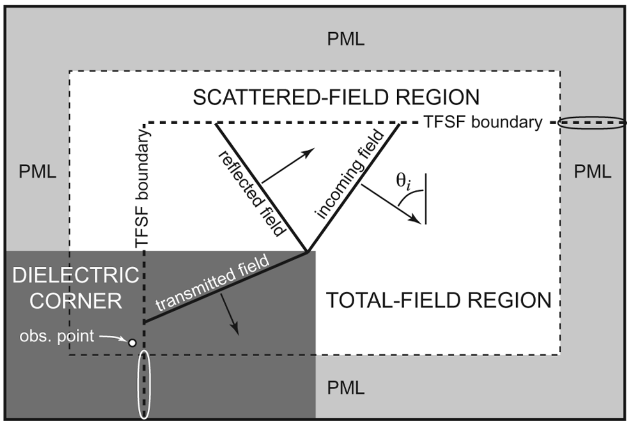


Fig. 6. A dielectric corner where the incident field originated in the halfspace region to the left. The incident field consists of the incoming field, the reflected field, and the transmitted field. There are two places where the TFSF boundary passes into the PML. These are indicated with an oval: one in the dielectric and one in free space.

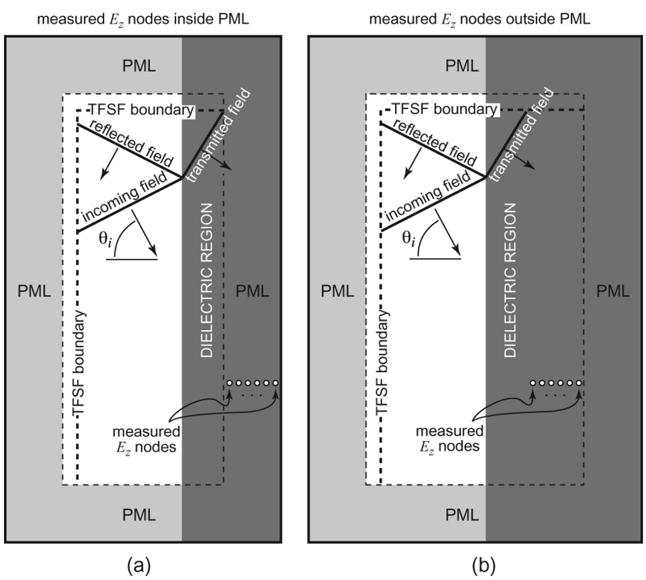


Fig. 7. Calibration set-up to determined the transfer function for the PML when the TFSF boundary is in the dielectric region. (a) The measured nodes are embedded inside the PML. (b) The measured nodes are outside the PML.

in Fig. 7. In this case the AFP method is used to introduce the incident field in a half-space problem (with no discontinuity in the dielectric). As drawn, the transfer functions obtained for the "measured" nodes in Fig. 7 would be used for the nodes adjacent to the TFSF boundary in the PML in the dielectric region shown at the bottom of Fig. 6. It is important to note that although the incoming and reflected field can be characterized by a single angle of incidence (or reflection), this is not true of the transmitted field. As described in [11], owing to the dispersion inherent in the FDTD grid, the angle of transmission is frequency dependent. Because of this, and the anisotropy of the FDTD grid, the calibration measurement is done in such a way as to reproduce this phenomenon. The distance between the PML and the interface is unimportant. As was done in Fig. 2, the field is measured both with and without the PML present at the measured nodes. Transforming from the time domain to the

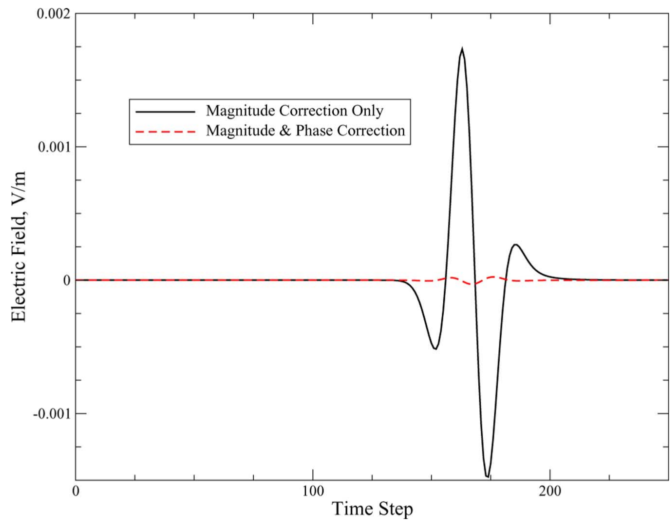


Fig. 8. Field at the observation point shown in Fig. 1 versus time. The simulation is constructed so that over the duration of the observation only the incoming field has passed into the PML. Since the observation point is in the scattered-field region, ideally the field would be zero.

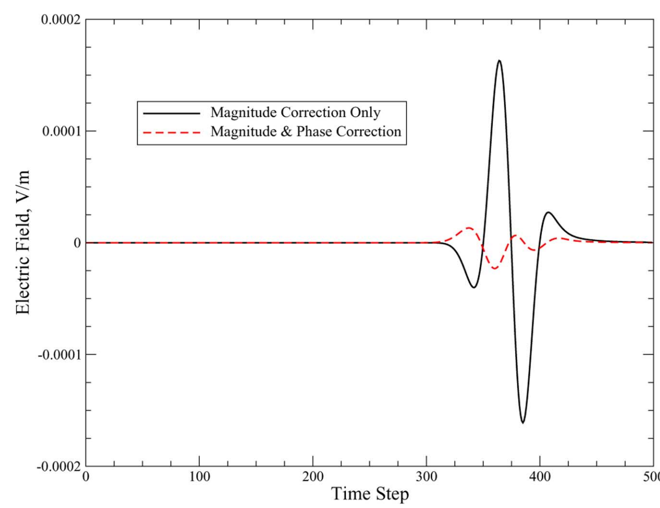


Fig. 9. Field at the observation point shown in Fig. 6 versus time. Similar to Fig. 8, the simulation is constructed so that over the duration of the observation only the transmitted field has passed into the PML. Since the observation point is in the scattered-field region, ideally the field would be zero.

frequency domain and then normalizing the PML-present measurement by the PML-absent measurement gives the transfer function. For the dielectric case we again find it is a sufficiently good approximation to treat the magnitude as a constant and model the phase variation as a linear function of frequency.

## IV. Results

There is an observation point indicated in the upper right portion of the scattered-field region in Fig. 1. This point is two points above the TFSF boundary and two points to the left of the start of the PML. Hence, ideally, the field at this point should be zero until scattered fields propagate to this point from a discontinuity in the total-field region. Fig. 8 shows the fields at this observation point when one does and does not account for the effect the PML has on the phase of the incident field. (Thus one plot corresponds to the field that is present using the original G-TFSF formulation and the other plot corresponds to the AFP-

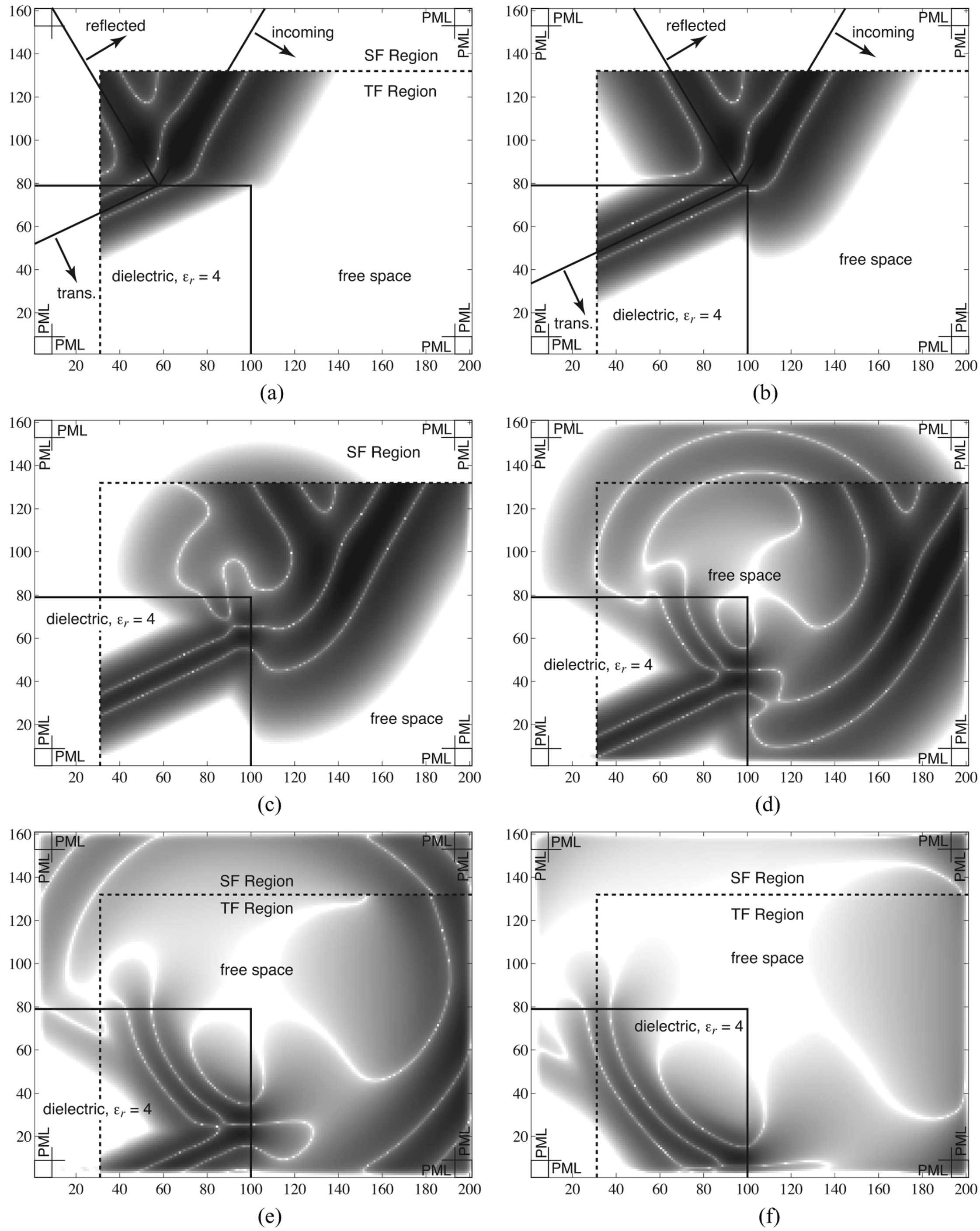


Fig. 10. Snapshots of a dielectric corner when the illumination originates in the half-space region to the left of the corner. These gray-scale images use four decades of logarithmic compression such that fields larger than one ten-thousandths of the peak value appear as non-white. Snapshots were taken at time step (a) 180, (b) 230, (c) 280, (d) 330, (e) 380, and (f) 430. See the text for further details.

based G-TFSF formulation being described here.) In the simulation the incoming field was a unit-amplitude Ricker wavelet discretized such that there were 20 points per wavelength at the most energetic frequency of the pulse. The simulation was run at the 2D Courant limit of $1/\sqrt{2}$ and the incident angle corresponds 60 degrees as drawn in Fig. 1. Over the duration shown here, no scattered fields from within the total-field region had arrived at that observation point. The fact that the fields at the observation point are non-zero is a consequence of the spurious leaking of the incoming field as it propagates along the portion of the TFSF boundary embedded in the PML.

If one corrects for only the magnitude change caused by the PML, the maximum of the spurious field is found to be $1.732 \times 10^{-3}$ V/m. On the other hand, by correcting for both the magnitude and phase change caused by the PML, the maximum of the spurious field drops to $3.037 \times 10^{-5}$ V/m, i.e., a reduction in the spurious field of slightly more than 35 dB.

Fig. 9 is similar to Fig. 8 except now the observation point is in the dielectric scattered-field region as indicated in Fig. 6. (The observation point appears in the lower left portion of the scattered-field region in Fig. 6.) This point is two cells above the PML and two cells to the left of the TFSF boundary. The incident angle is 60 degrees and the relative permittivity of the dielectric is 4. The simulation is run at the 2D Courant limit and the incident field is a unit amplitude Ricker wavelet discretized such that there are 40 points per wavelength at the most energetic frequency in free space (thus there are 20 points per wavelength in the dielectric). Fig. 9 shows the electric field at the observation point when there is a correction of only the magnitude and when there is a correction of magnitude and phase. Again, the ideal solution is the absence of any field.

The improvement observed in Fig. 9 by incorporating the phase information is not as dramatic as in Fig. 8. In this case, when only the magnitude is corrected, the maximum of the spurious field is $1.630 \times 10^{-4}$ V/m. When the phase is also corrected, the maximum drops to $2.308 \times 10^{-5}$ V/m. This represents an improvement of slightly less than 17 dB.

Fig. 10 shows snapshots of a simulation in which a pulsed, unit-amplitude, $\mathrm{TM}_z$ polarized Ricker wavelet plane wave illuminates a dielectric corner. This illumination, discretization, and dielectric constant are the same as described for the calibration measurement. The illumination starts in the half-space region. The TFSF boundary is two-sided and the incident field, consisting of the incoming, reflected, and transmitted waves, emerges from the TFSF "fully formed" for the half-space problem [8], [9], [11], [12]. The computational domain is $201 \times 161$ cells. The figures are drawn to scale and the locations of the TFSF boundary, the dielectric, and the PML are indicated. The PML is eight cells thick and spans the edges of the grid (even though, for clarity, the PML is only explicitly draw in the corners). These snapshots use four decades of logarithmic compression such that any field greater than one ten-thousandth of the peak field will show up as non-white.

Fig. 10(a) shows the field at time-step 180 when the leading edge of the incoming field has arrived at the discontinuity at the corner. This figure indicates the direction of travel of the incoming, reflected, and transmitted waves by drawing a line along planes of constant phase. For the sake of illustration, these lines are extended into the scattered-field region even though there is no incident field in this region. Fig. 10(c) shows the field at time-step 280 when the incoming field has propagated beyond the right side of the grid. The important thing to notice is that there is no leaked field visible in the scattered-field region—the only fields present in the scattered-field region are those associated with the scattering from the corner. Fig. 10(d) and (e), taken at time-steps 330 and 380, respectively, show the fields after the transmitted wave has encountered the bottom PML. Although difficult to see, close inspection of these figures shows faint non-white patches adjacent to the TFSF boundary. However, these patches are confined to the PML region—there is no visible leakage into the interior of the grid.

One additional note is that the AFP technique is able to provide the incident field at any point in the grid (i.e., the incident field that would exist without the discontinuity). Thus, even for points within the total-field region, one can obtain the scattered field simply by subtracting the incident field provided by the AFP method.

## V. Conclusion

We have shown that the G-TFSF concept can be folded into an AFP TFSF framework. By incorporating both magnitude and phase information about the effect the PML has on the incident field, one can simply terminate the TFSF boundary at the edge of the computational grid—there is no need for a four-sided TFSF boundary. This new approach also ensures less leakage while using smaller PML regions than used in the original G-TFSF work.

## References


[1] D. E. Merewether, R. Fisher, and F. W. Smith, "On implementing a numeric Huygen's source scheme in a finite difference program to illuminate scattering bodies," *IEEE Trans. Nucl. Sci.*, vol. 27, no. 6, pp. 1829–1833, Dec. 1980.

[2] K. R. Umashankar and A. Taflove, "A novel method to analyze electromagnetic scattering of complex objects," *IEEE Trans. Electromagn. Compat.*, vol. EMC-24, no. 4, pp. 397–405, Nov. 1982.

[3] A. Taflove and S. Hagness, *Computational Electrodynamics: The Finite-Difference Time-Domain Method*, 3 ed. Boston, MA: Artech House, 2005.

[4] C. Guiffaut and K. Mahdjoubi, "Perfect wideband plane wave injector for FDTD method," in *Proc. IEEE Antennas and Propagat. Soc. Int. Symp.*, Salt Lake City, UT, Jul. 2000, vol. 1, pp. 236–239.

[5] U. Oguz and L. Gürel, "Interpolation techniques to improve the accuracy of the plane wave excitations in the finite difference time domain method," *Radio Sci.*, vol. 32, no. 6, pp. 2189–2199, Nov.–Dec. 1997.

[6] U. Oguz and L. Gürel, "An efficient and accurate technique for the incident-wave excitations in the FDTD method," *IEEE Trans. Microwave Theory Tech.*, vol. 46, no. 6, pp. 869–882, Jun. 1998.

[7] T. Tan and M. Potter, "1-d multipoint auxiliary source propagator for the total-field/scattered-field FDTD formulation," *IEEE Antennas Wireless Propag. Lett.*, vol. 6, pp. 144–148, 2007.

[8] T. Martin and L. Pettersson, "Modified fresnel coefficients for Huygen's sources in FDTD," *Appl. Comput. Electromagn. Society J.*, vol. 17, no. 1, pp. 30–41, Mar. 2002.

[9] C. D. Moss, F. L. Teixeira, and J. A. Kong, "Analysis and compensation of numerical dispersion in the FDTD method for layered, anisotropic media," *IEEE Trans. Antennas Propag.*, vol. 50, no. 9, pp. 1174–1184, Sep. 2002.

[10] J. B. Schneider, "Plane waves in FDTD simulations and a nearly perfect total-field/scattered-field boundary," *IEEE Trans. Antennas Propag.*, vol. 52, no. 12, pp. 3280–3287, Dec. 2004.

[11] J. B. Schneider and K. Abdijalilov, "Analytic field propagation TFSF boundary for FDTD problems involving planar interfaces: PECs, TE, and TM," *IEEE Trans. Antennas Propag.*, vol. 54, no. 9, pp. 2531–2542, Sep. 2006.

[12] K. Abdijalilov and J. B. Schneider, "Analytic field propagation TFSF boundary for FDTD problems involving planar interfaces: Lossy material and evanescent fields," *IEEE Antennas Wireless Propag. Lett.*, vol. 5, pp. 454–458, 2006.

[13] A. Taflove, "Review of the formulation and applications of the finite-difference time-domain method for numerical modeling of electromagnetic wave interactions with arbitrary structures," *Wave Motion*, vol. 10, no. 6, pp. 547–582, 1988.

[14] J. B. Schneider and C. L. Wagner, "FDTD dispersion revisited: Faster-than-light propagation," *IEEE Microw. Guided Wave Lett.*, vol. 9, no. 2, pp. 54–56, Feb. 1999.

[15] V. Anantha and A. Taflove, "Efficient modeling of infinite scatterers using a generalized total-field/scattered-field FDTD boundary partially embedded within PML," *IEEE Trans. Antennas Propag.*, vol. 50, no. 10, pp. 1337–1349, Oct. 2002.

[16] J.-P. Bérenger, "A perfectly matched layer for the absorption of electromagnetic waves," *J. Comput. Phys.*, vol. 114, no. 2, pp. 185–200, 1994.

[17] J. A. Roden and S. D. Gedney, "Convolution PML (CPML): An efficient FDTD implementation of the CFS-PML for arbitrary media," *Microw. Opt. Technol. Lett.*, vol. 27, no. 5, pp. 334–339, Dec. 2000.

[18] Z. Wu and J. Fang, "High-performance PML algorithms," *IEEE Microw. Guided Wave Lett.*, vol. 6, no. 9, pp. 335–337, Sep. 1996.

[19] W. C. Chew and J. M. Jin, "Perfectly matched layers in the discretized space: An analysis and optimization," *Electromagnetics*, vol. 16, no. 4, pp. 325–340, 1996.

[20] J. Fang and Z. Wu, "Closed-form expression of numerical reflection coefficient at PML interfaces and optimization of PML performance," *IEEE Microw. Guided Wave Lett.*, vol. 6, no. 9, pp. 332–334, Sep. 1996.

[21] J.-P. Bérenger, "Evanescent waves in PML's: Origin of the numerical reflection in wave-structure interaction problems," *IEEE Trans. Antennas Propag.*, vol. 47, no. 10, pp. 1497–1503, Oct. 1999.

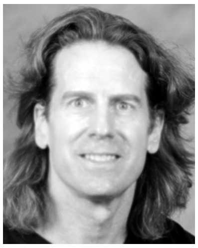

**John B. Schneider** (M'91–SM'10) received the B.S. degree in electrical engineering from Tulane University, New Orleans, LA, and the M.S. and Ph.D. degrees in electrical engineering from the University of Washington, Seattle.

He is presently an Associate Professor in the School of Electrical Engineering and Computer Science, Washington State University, Pullman. His research interests include the use of computational methods to analyze acoustic, elastic, and electromagnetic wave propagation.

Prof. Schneider is a former recipient of the Office of Naval Research Young Investigator Award. He has served as an Associate Editor of the *Journal of the Acoustical Society of America* and is the Co-Chair of the Technical Program Committee for the 2011 IEEE International Symposium on Antennas and Propagation in Spokane, Washington.

**Zhen Chen** (S'09) was born in Changsha, China, in 1987. He received the B.S. degree (with high distinction) from Huazhong University of Science and Technology Wuhan, China, in 2009.

He is currently a Research Assistant at Washington State University, Pullman, where he is pursuing a doctoral degree involving the application and enhancement of the finite-difference time-domain method.